

Nickel–Zinc Ferrite Nanoparticles for Hyperthermia: Preserving Superparamagnetism Across a Broad Range of Particle Sizes

Minh Dang Nguyen, Supun B. Attanayake, Pailinrut Chinwangso, Supawitch Hoijang, Chengzhen Qin, Jiming Bao, Manh-Huong Phan,* and T. Randall Lee*



Cite This: *ACS Appl. Mater. Interfaces* 2025, 17, 22929–22940



Read Online

ACCESS |



Metrics & More



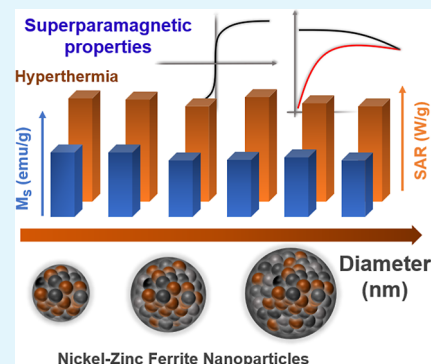
Article Recommendations



Supporting Information

ABSTRACT: Nickel–zinc ferrite (NZF) compounds, renowned for their mixed spinel structures, hold significant promise for diverse applications in high-frequency devices and biomedicine. This study utilizes solvothermal synthesis to produce NZF nanoparticles (NPs) with tunable diameters ranging from 40 to 300 nm. These NZF NPs exhibit polycrystalline structures, with crystallite sizes tailored to be approximately 8 nm, a pivotal factor in preserving their superparamagnetic (SPM) properties across a broad size spectrum. A combination of scanning electron microscopy (SEM), transmission electron microscopy (TEM), X-ray diffraction (XRD), Raman spectroscopy, energy-dispersive X-ray spectroscopy (EDS), inductively coupled plasma mass spectrometry (ICP–MS), and X-ray photoelectron spectroscopy (XPS) confirms the structures and compositions of the synthesized samples. Magnetometry measurements revealed consistent saturation magnetization (M_s) values and SPM features at room temperature across all samples, despite variations in particle size. These nanoparticles transition to a ferrimagnetic (FiM) or blocked state at approximately 150 K. Consequently, comparable specific absorption rate (SAR) values are achieved across the samples, which can be attributed to the uniformity in the size of the primary crystallites (crystallite size ~ 8 nm) within the polycrystalline structures of the NZF nanoparticles. Our study underscores the significance of controlling the crystallite sizes in polycrystalline ferrite nanoparticles, enabling the attainment of desirable SPM and hyperthermia responses across a wide size spectrum. It also delineates an effective methodology for producing NZF nanoparticles suitable for a variety of applications, including optoelectronic and high-frequency devices, photocatalysis, environmental remediation, sensor systems, and advanced biomedical technologies.

KEYWORDS: superparamagnetic properties, nickel zinc ferrites, spinel ferrites, magnetic hyperthermia, high-frequency applications



INTRODUCTION

Spinel ferrites, denoted by the formula $M\text{Fe}_2\text{O}_4$, have become prominent magnetic materials utilized across a broad spectrum of applications, including catalysis, photocatalysis, environmental remediation, electronics, optoelectronics, and biomedicine.^{1–3} Among these, Nickel–zinc ferrites (NZF), typically formulated as $\text{Ni}_x\text{Zn}_{1-x}\text{Fe}_2\text{O}_4$, have attracted considerable interest in recent years due to their unique physical characteristics. These include high magnetic permeability, high resistivity, high Curie temperature, and semiconducting properties.⁴ These properties render NZF nanomaterials particularly useful in high-frequency applications, such as high-frequency circuits, high-quality filters, and read-write heads for high-speed digital devices, as well as in biomedical applications, including magnetic hyperthermia and magnetic resonance imaging.^{4–10}

In addition to these applications, recent studies have explored the potential of NZF nanomaterials in microwave absorption, electromagnetic shielding, gas sensing, water treatment, supercapacitors, lithium-ion batteries, catalysts, and photocatalysis.^{11–16} Structural parameters such as size

and shape are critical in influencing the properties of nanomaterials and can be precisely tailored through chemical synthesis.¹⁷ Furthermore, the application of nanoparticles (NPs) often requires additional fabrication or functionalization steps, such as dispersion in a medium or coating with functional entities, thereby making the particle size a key parameter in the successful deployment of nanomaterials. Consequently, developing a reliable synthetic method to produce NZF NPs with tunable sizes is crucial for elucidating the physical properties of the materials and enhancing the performance of nanomaterials in their targeted applications. A pertinent question remains concerning the feasibility of tuning the size across a broad range while effectively maintaining the superparamagnetic (SPM) properties of NZF NPs.

Received: January 12, 2025

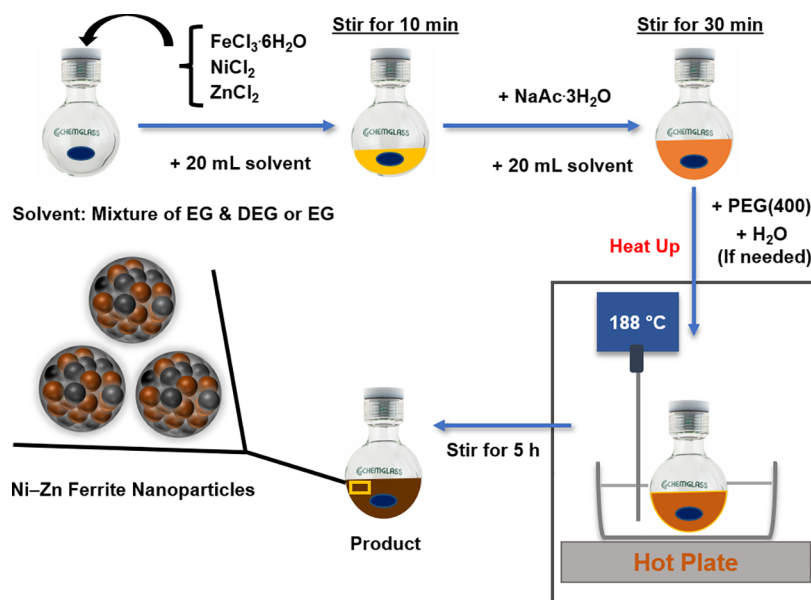
Revised: March 20, 2025

Accepted: March 23, 2025

Published: April 2, 2025



Scheme 1. Strategy for Synthesizing Nickel–Zinc Ferrite Nanoparticles (NZF NPs) with Tunable Diameter Dimensions from 40 to 300 nm



To date, various methods have been reported for synthesizing NZF nanomaterials, including coprecipitation, autocombustion, mechanical milling combined with sintering, sol–gel autoignition, thermal decomposition, and nonaqueous methods.^{4,18–26} Yet, few synthetic approaches can fabricate NZF NPs with uniform particle structures while also allowing for size tunability across a wide range. Some progress has been made using the reverse micelle method, hydrothermal method, solvothermal reflux, and sol–gel method,^{27–32} but the achievable nanoparticle diameters have predominantly been limited to below 50 nm, with restricted size tunability. A synthetic method capable of producing uniform particle structures and tuning the diameters of NZF NPs from 50 to several hundred nanometers is desirable for both fundamental studies and diverse applications. In this size range, magnetic NPs can retain the advantageous SPM properties if the constituent crystallite sizes are controlled to be less than 15 nm,^{17,33–35} which are useful for biosensing and biomedical applications.

In this study, we introduce a solvothermal synthetic route for synthesizing NZF NPs with tunable diameters ranging from 40 to 300 nm. The NZF NPs possess polycrystalline structures composed of primary crystals sized ~ 8 nm, which is crucial for preserving the SPM features of the NPs. These NPs were comprehensively characterized using scanning electron microscopy (SEM), transmission electron microscopy (TEM) with selected area electron diffraction (SAED), and X-ray diffraction (XRD) to elucidate their structural and crystalline characteristics. Raman spectroscopy and X-ray photoelectron spectroscopy (XPS) provided further insights into the compositional features of the NPs, while energy-dispersive X-ray spectroscopy (EDS) and inductively coupled plasma mass spectrometry (ICP–MS) were employed to determine their chemical composition. The magnetic properties of the NZF NPs were measured using a vibrating sample magnetometer (VSM) integrated within the physical property measurement system (PPMS), affirming their SPM properties and comparable saturation magnetization levels. As a result, we achieved comparable magnetic hyperthermia responses of the NZF NPs

across a broad size range from 40 to 300 nm. With its capability for size tunability and effective preservation of SPM properties, the method presented in this research holds promise for producing NZF NPs suitable for a wide range of applications.

EXPERIMENTAL SECTION

Materials. For the synthesis of NZF NPs, iron(III) chloride hexahydrate ($\text{FeCl}_3 \cdot 6\text{H}_2\text{O}$) (97%; Alfa Aesar), nickel(II) chloride anhydrous (NiCl_2 ; Sigma-Aldrich), and zinc(II) chloride anhydrous (ZnCl_2 ; $\geq 98\%$; Sigma-Aldrich) were used as precursors. The solvents employed were ethylene glycol (EG) (99%; Sigma-Aldrich) and diethylene glycol (DEG) (99%; ACROS Organics). Sodium acetate trihydrate ($\text{NaAc} \cdot 3\text{H}_2\text{O}$) (99%) was purchased from Fisher. Surfactant polyethylene glycol-400 (PEG(400)) was purchased from Sigma-Aldrich. Deionized water with a resistance of $18\text{ M}\Omega\text{-cm}$ was produced using an Academic Milli-Q Water System (Millipore Corporation). A pressure vessel with a volume of 65 mL from ChemGlass was utilized for the synthesis of NZF NPs.

Synthesis of Nickel–Zinc Ferrite Nanoparticles. The synthesis method for NZF NPs was adapted from a previously reported method for the synthesis of iron oxide (Fe_3O_4) NPs, with modifications.³³ The process involved charging NiCl_2 (0.162 g, 1.25 mmol), ZnCl_2 (0.170 g, 1.25 mmol), and $\text{FeCl}_3 \cdot 6\text{H}_2\text{O}$ (1.350 g, 5 mmol) precursors into the pressure vessel and applying magnetic stirring to dissolve them in 20 mL of solvent. The solvent used was either 40 mL of EG or a 40 mL mixture of EG and DEG. Subsequently, 3.6 g of $\text{NaAc} \cdot 3\text{H}_2\text{O}$ and the remaining 20 mL of solvent were added, followed by stirring for 30 min to form a homogeneous mixture. Then, an aliquot of 1.2 mL PEG (400) surfactant and water (if needed) were added. The pressure vessel was sealed tightly, heated to $188\text{ }^\circ\text{C}$, and the reaction was maintained for 5 h. After the reaction, the product was allowed to cool naturally and washed at least three times with ethanol. For each washing cycle, the NPs were dispersed in ethanol in an ultrasonic bath for 15 min, followed by magnetic separation. To control the diameter of the NPs, varying ratios of the binary solvent system or the addition of water were used. By changing the solvent compositions from 15/25 mL, 20/20 mL, to 40/0 mL of EG/DEG, the sizes of the NZF NPs were controlled to average diameters of 41, 70, and 307 nm, respectively. Adding different amounts of water, such as 0.5 mL, 1.0 mL, and 1.25 mL, helped to reduce the size from 307 to 201, 136, and 107 nm,

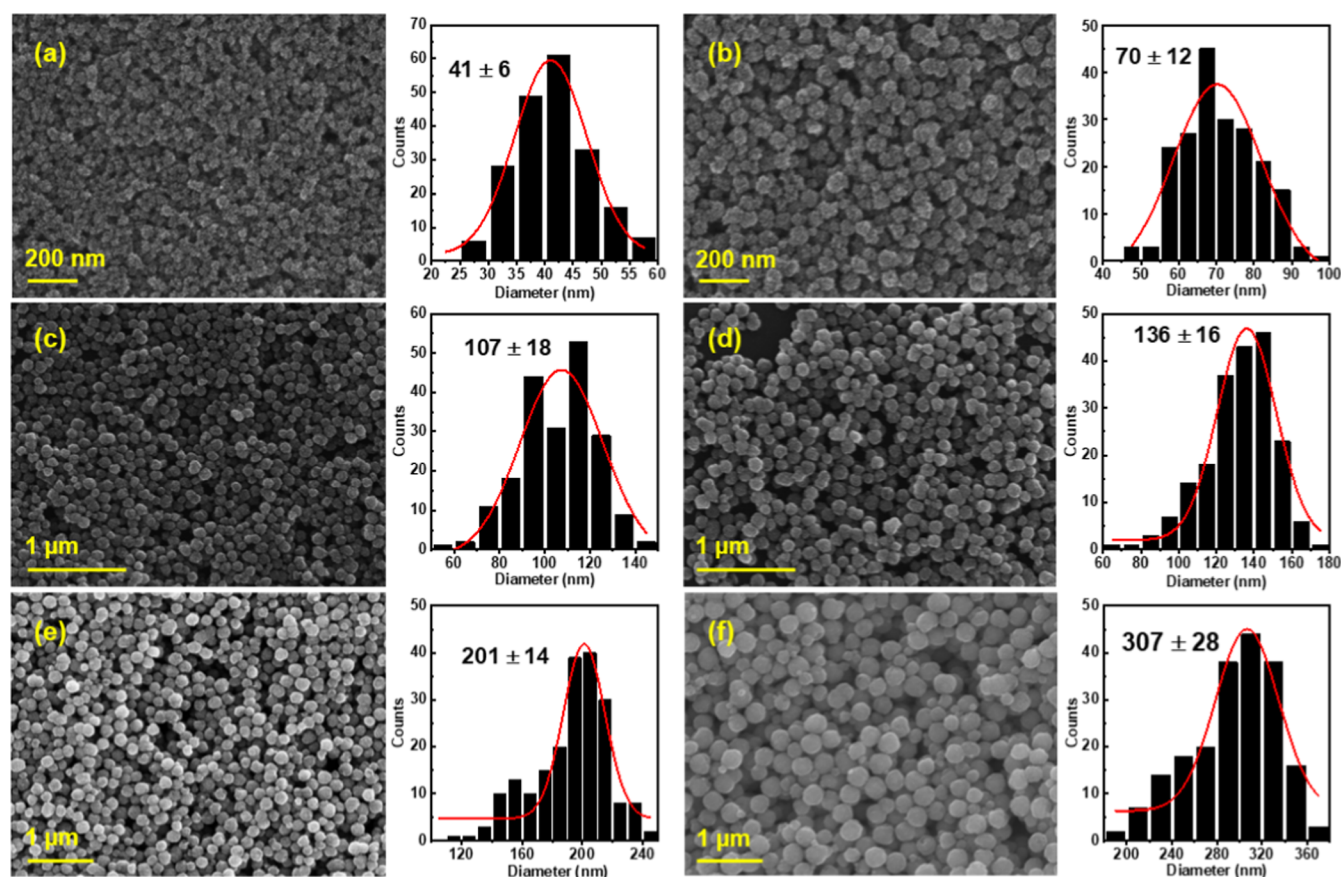


Figure 1. SEM images and size distribution of NZF NPs with average diameters of (a) 41, (b) 70, (c) 107, (d) 136, (e) 201, and (f) 307 nm.

respectively. The heating rate was maintained at around 5 °C/min with a consistent stirring speed of 750 rpm under all conditions. It is noteworthy that by following this strategy, we could achieve NZF NPs with diameters ranging from 40 to 300 nm. Scheme 1 illustrates the procedure used for synthesizing NZF NPs with tunable diameters.

Materials Characterization. For imaging all synthesized NPs, a FEI Dual Beam 235 focused ion beam (FIB), scanning electron microscope (SEM), and a JSM-6330F scanning electron microscope (SEM) operating at a voltage of 15 kV were used to observe the morphology of the NPs. All samples were dispersed in ethanol and drop-cast onto cleaned silicon wafers for analysis. The NPs were further characterized using a JEOL JEM-2010F transmission electron microscope (TEM) for high-resolution imaging and selected area electron diffraction (SAED) at an accelerating voltage of 200 kV was used to assess the SAED patterns. The dispersed NZF NPs in ethanol were dropped onto 300-mesh holey carbon-coated copper grids for TEM characterization. A powder X-ray diffractometer (PXRD) (Smart Lab, Rigaku), operating with Cu K α radiation at 40 kV and 44 mA, was used to determine the phase composition and crystallinity of the NPs. Powder samples were prepared on a clean glass slide surface for measurement. Raman spectroscopy was conducted using a wavelength of 532 nm, 10 \times magnification, and 1.5 mW laser power. X-ray photoelectron spectroscopy (XPS) was performed using a PHI 5700 X-ray photoelectron spectrometer with a monochromatic Al K α X-ray source to characterize the NZF NPs. For XPS data analysis, the C 1s peak at a binding energy of 284.8 eV was used for calibration. Energy-dispersive X-ray spectroscopy (EDS) data were collected using the JSM-6330F SEM. The chemical compositions of the NPs were determined using inductively coupled plasma mass spectrometry (Agilent 8800 QQQ-ICP-MS). The magnetic properties of the NZF NPs were characterized by utilizing the vibrating sample magnetometer (VSM) option in a Quantum Design DynaCool Physical Property Measurement System (PPMS). The magnetic hyperthermia responses of the NZF NPs were assessed using 4.2 kW Ambrell

Easyheat Li3542 equipment with varying AC magnetic fields (0–800 Oe) at a constant frequency of 310 kHz. The specific absorption rate (SAR) value was used as an index to reflect the efficiency of heating performance, with a higher SAR value corresponding to higher heating efficiency. The equation for calculating SAR values is $SAR = (\Delta T/\Delta t)/(C_p/\rho)$, where $\Delta T/\Delta t$ is determined from the slope of the heating curve, C_p represents the heat capacity of the liquid solvent (4.186 J/g·K for water), and ρ is a unitless quantity representing the mass of magnetic material per unit mass of liquid solvent.

RESULTS AND DISCUSSION

Structure and Compositions of Nickel–Zinc Ferrite Nanoparticles. The size of the NPs was effectively controlled by varying the solvent compositions or adding a small amount of water. Figure 1 displays the SEM images of the NZF NPs and their corresponding diameter size distribution, which was obtained by counting 200 nanoparticles and then fitting the data with a Gaussian function. As shown in Figure 1, the NPs exhibit a uniform size and spherical-like shape. Larger particles tend to exhibit a rounder geometry. Bulkier solvent molecules, such as DEG, can slow down the agglomeration of primary crystals, effectively reducing the size of the NPs.^{35,36} Sample diameters of 41 ± 6 nm, 70 ± 12 nm, and 307 ± 28 nm were prepared using solvent systems of 15 mL EG/25 mL DEG, 20 mL EG/20 mL DEG, and 40 mL EG, respectively. By maintaining the same synthetic conditions that achieved a sample diameter of 307 nm, the addition of 0.5 mL, 1 mL, and 1.25 mL of water reduced the diameter of the NPs to 201, 136, and 107 nm, respectively. This reduction in size with the addition of more water is consistent with observations made in the synthesis of magnetite nanoparticles.^{33,37}

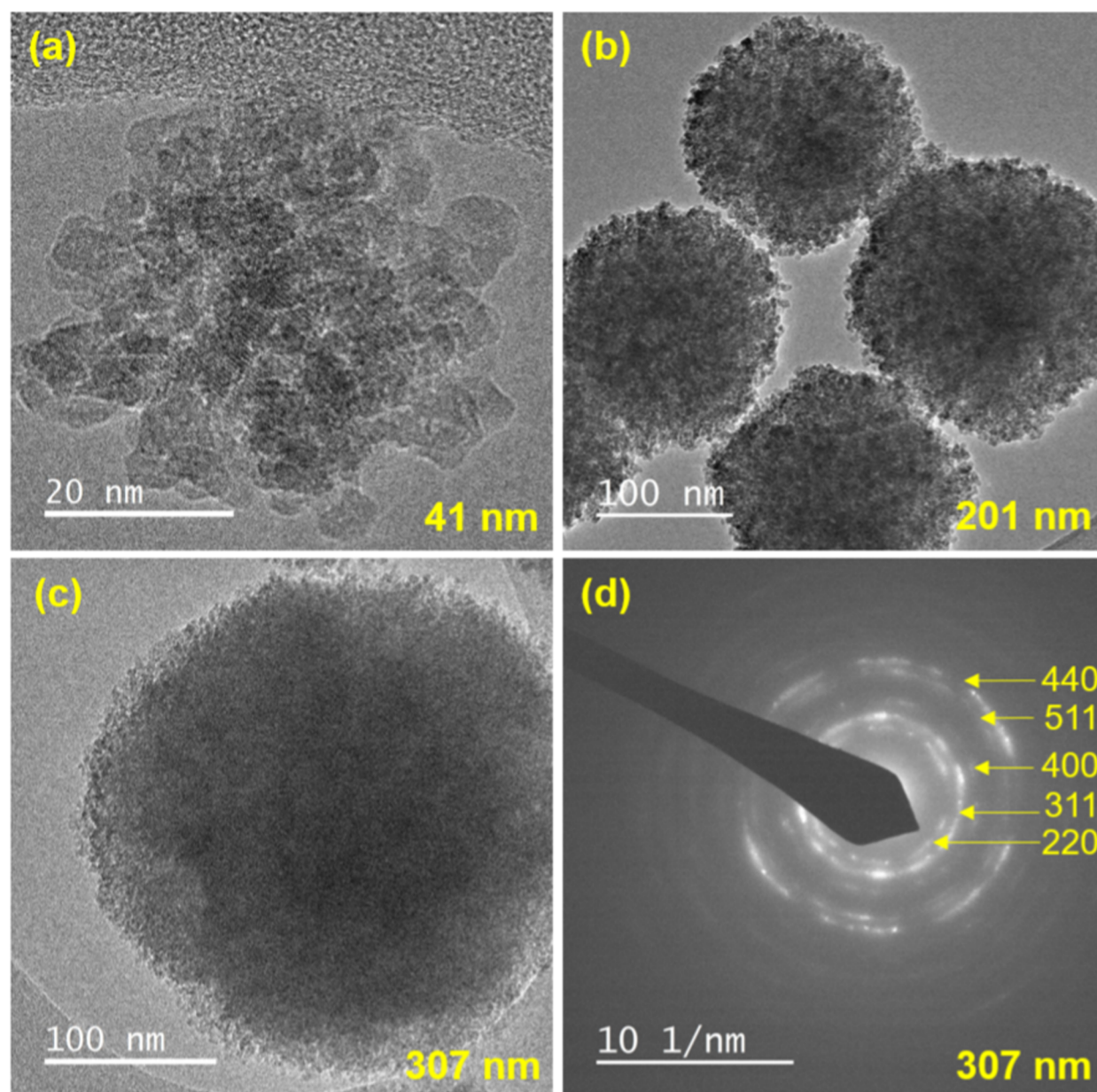


Figure 2. TEM images of NZF NPs with average diameters of (a) 41, (b) 201, and (c) 307 nm; and (d) SAED pattern of the 307 nm sample.

The TEM imaging provides detailed insights into the structures of the synthesized NZF NPs. Figure 2 showcases TEM images of sample diameters 41, 201, and 307 nm. The images clearly show that each particle comprises numerous primary crystals. These primary crystals, having random shapes, are stacked together to form the larger polycrystalline structure of the particle. Due to the random morphology of the crystals, smaller NPs, such as the 41 nm sample, do not exhibit a perfectly spherical shape. However, larger particles tend to adopt a more rounded morphology. The SAED pattern of a single particle, approximately 307 nm in size, is presented in Figure 2d. The ring pattern confirms the polycrystalline structure. The rings are not continuous circles but are observed as collections of many bright segments, which together create a ring shape. This indicates that the primary crystals were stacked together in a specific preferred orientation. A purely random stacking of crystals would result in a continuous ring feature in the SAED pattern.

The XRD was used to analyze the phase composition of the NPs and to estimate their crystallinity. All samples exhibited six prominent peaks, which can be attributed to the planes (111), (220), (311), (400), (511), and (440), as specified in Figure 3a. The XRD patterns confirm that all samples are consistent with spinel ferrite materials. The crystallite size (also referred to as “grain size”) was calculated and specified in Table S1. The crystallite sizes ranged from around 8 nm, corroborating the polycrystalline structures of the samples, in accordance with the TEM and SAED results. The structure of the NPs can be envisioned as clusters of numerous primary crystals with approximately 7 to 9 nm in size, indicating that all samples possess comparable levels of crystallinity. Despite the large overall size of the particles, the crystallite sizes, around 8 nm, are significantly smaller than the critical size for transitioning from SPM to ferrimagnetic behavior, which is approximately 25 nm for Fe_3O_4 and 28 nm for nickel ferrite (NiFe_2O_4).^{17,38} To date, no report has specified the SPM size of NZF

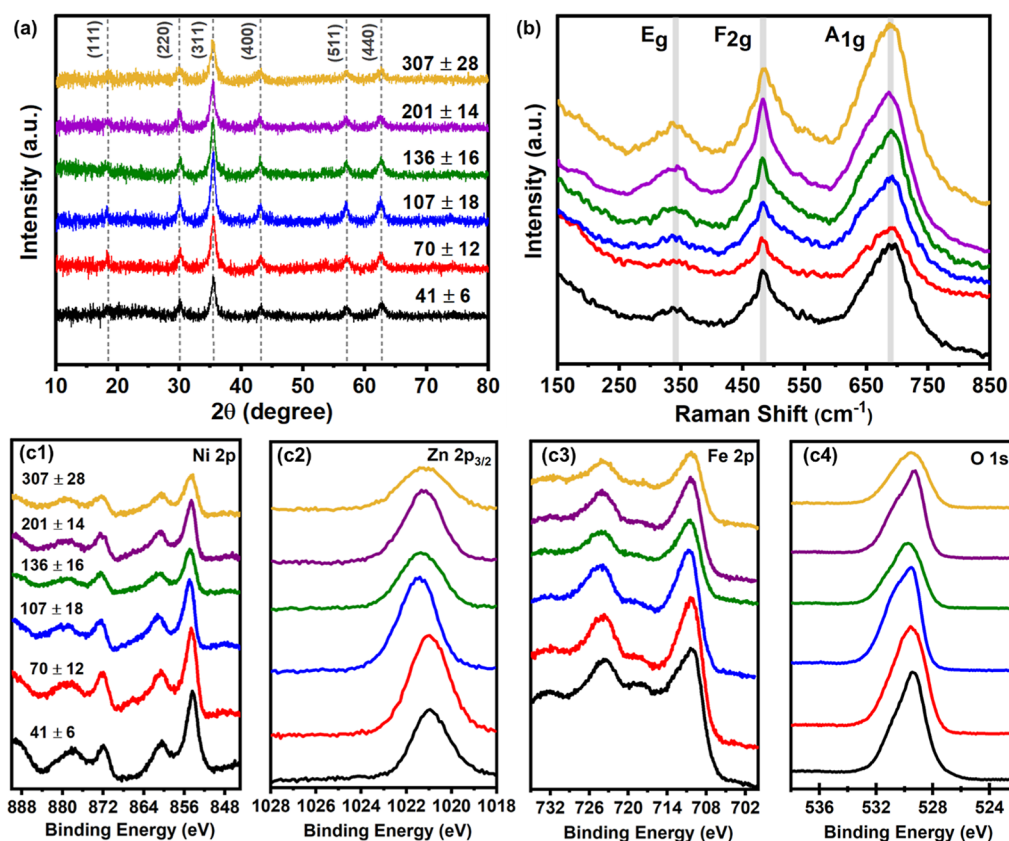


Figure 3. (a) XRD patterns, (b) Raman spectra, and (c1–c4) high-resolution XPS spectra of Ni 2p, Zn 2p_{3/2}, Fe 2p, and O 1s for NZF NPs with average diameters ranging from 41 to 307 nm.

nanocrystals; however, experimental results have shown the SPM properties in NZF nanocrystals up to 19 nm, as reported by Li's group³⁹ and Rhee's group.²⁸ Thus, despite the larger size of the synthesized NZF NPs, the magnetic properties of the polycrystalline NPs are expected to exhibit SPM behavior due to the small size of the primary crystals (crystallite size <10 nm). While maintaining small crystallite sizes to achieve SPM properties, the diffraction peaks in the XRD patterns broaden. Consequently, the broadened high-intensity (311) peak can overwhelmingly suppress the appearance of the nearby minor (222) peak in the XRD pattern. This phenomenon is consistently observed in large superparamagnetic iron oxide superparticles.³⁴ However, the (222) peak can be detected through the deconvolution of the major (311) peak (see Figure S1). The crystallite sizes calculated from the (311) peak after deconvolution were 8.7, 8.1, 9.2, 9.1, 8.7, and 7.7 nm for NZF NPs with sizes of 40, 70, 107, 136, 201, and 307 nm, respectively, closely matching the results presented in Table S1.

To further confirm the success of the synthesis in the composition of NZF NPs, Raman spectroscopy and XPS were conducted. Figure 3b presents the Raman spectra of the NZF NPs, which display three prominent broad peaks observed at approximately 690, 480, and 330 cm⁻¹. These peaks can be assigned to the A_{1g} symmetric stretching mode, F_{2g} asymmetric bending vibration, and E_g symmetric bending vibrations.^{20,23,40–42} In Ni_xZn_{1-x}Fe₂O₄ compounds, varying the x values typically causes a noticeable shift in the Raman peaks.^{22,41} However, no significant shift was observed across all six samples in these spectra, indicating highly uniform chemical compositions. Figure 3c1–c4 presents the high-

resolution XPS spectra of Ni 2p, Zn 2p_{3/2}, Fe 2p, and O 1s, confirming the presence of Ni and Zn in the ferrites and the homogeneity of the nanoparticle compositions. The main principal peaks of Ni 2p were observed at around 854.6 eV for Ni 2p_{3/2} and 872.0 eV for Ni 2p_{1/2}, with satellite peaks noted at approximately 860.4 and 878.4 eV. The Ni 2p_{3/2} peak at approximately 854.6 eV is commonly assigned to Ni²⁺ in nickel oxides, nickel hydroxide, and nickel oxyhydroxides.⁴³ The shape of the Ni 2p spectra replicates the features of Ni 2p spectra observed in hydroxides and nickel ferrites.⁴⁴ The Zn 2p_{3/2} peak, observed at around 1021 eV, indicates the presence of Zn²⁺ in the structures.⁴⁵ The Fe 2p spectra show peaks at approximately 710.5, 724, and 718 eV, assigned to Fe 2p_{3/2}, Fe 2p_{1/2}, and the satellite peak of common ferrites, respectively.⁴⁶ The O 1s peak at around 529.5 eV is characteristic of oxygen in metal oxides and is accompanied by a minor peak at around 531 eV for metal–oxygen bonds and a minor peak at approximately 529.5 to 530 eV for surface species such as chemisorbed oxygen, hydroxyl groups, or chemical species on the spinel surface.⁴⁴

Chemical Formula of Nickel–Zinc Ferrite Nanoparticles. The synthesized NPs were characterized by the EDS and ICP–MS to accurately determine their chemical compositions. Table S2 presents the atomic percentages derived from EDS data. The presence of Si in the samples was attributed to the sample preparation on silicon wafers. From these atomic percentages, the atomic ratios were calculated to deduce the chemical formula. Table S3 shows the atomic percentages of component elements, calculated from the weight percent data provided by ICP–MS. Notably, since ICP–MS cannot measure the weight percent of oxygen,

Table 1. Chemical Formula of NZF NPs^a

diameter (nm)	theoretical Formula	EDS derived Formula	ICP–MS derived Formula
41 ± 6	Ni _{0.5} Zn _{0.5} Fe ₂ O ₄	Ni _{0.52} Zn _{0.23} Fe _{2.25} O ₄	Ni _{0.57} Zn _{0.24} Fe _{2.19} O ₄
70 ± 12	Ni _{0.5} Zn _{0.5} Fe ₂ O ₄	Ni _{0.54} Zn _{0.28} Fe _{2.18} O ₄	Ni _{0.58} Zn _{0.28} Fe _{2.14} O ₄
107 ± 18	Ni _{0.5} Zn _{0.5} Fe ₂ O ₄	Ni _{0.50} Zn _{0.31} Fe _{2.19} O ₄	Ni _{0.55} Zn _{0.34} Fe _{2.11} O ₄
136 ± 16	Ni _{0.5} Zn _{0.5} Fe ₂ O ₄	Ni _{0.52} Zn _{0.32} Fe _{2.16} O ₄	Ni _{0.55} Zn _{0.34} Fe _{2.11} O ₄
201 ± 14	Ni _{0.5} Zn _{0.5} Fe ₂ O ₄	Ni _{0.51} Zn _{0.34} Fe _{2.15} O ₄	Ni _{0.55} Zn _{0.32} Fe _{2.13} O ₄
307 ± 28	Ni _{0.5} Zn _{0.5} Fe ₂ O ₄	Ni _{0.52} Zn _{0.30} Fe _{2.18} O ₄	Ni _{0.56} Zn _{0.30} Fe _{2.14} O ₄

^aChemical formula Ni_xZn_yFe_zO₄ with $x + y + z = 3$; $y/z = \text{Zn/Fe}$ ratio; and $x/z = \text{Ni/Fe}$ ratio. The calculated values of x , y , and z were rounded off to two decimal places.

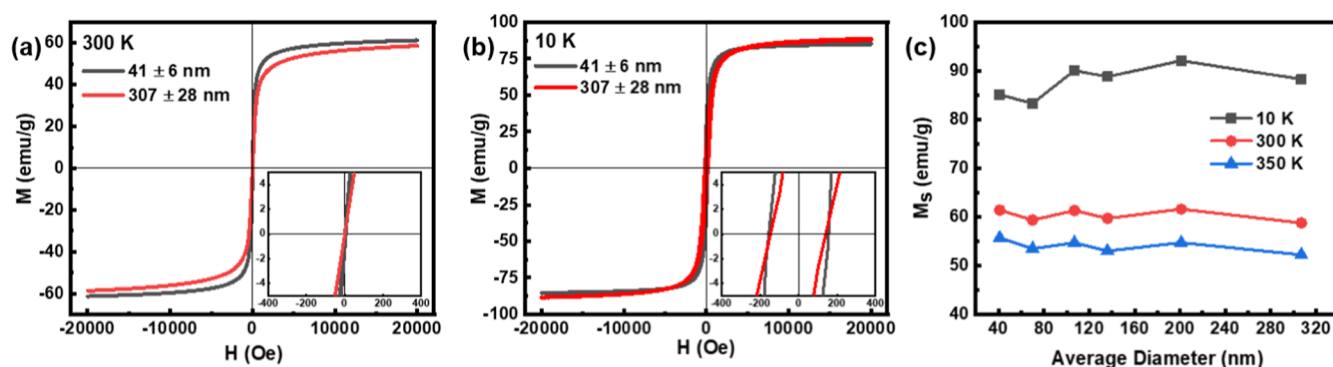


Figure 4. Field dependence of magnetization $M(H)$ curves for sample diameters 41 ± 6 nm and 307 ± 28 nm at (a) 10 K and (b) 300 K; (c) Saturation magnetization (M_s) versus particle diameter for all samples at temperatures of 10, 300, and 350 K.

Table 2. Magnetic Properties of NZF NPs

diameter (nm)	C_s (nm)	M_s (emu/g) (350 K)	M_s (emu/g) (300 K)	M_s (emu/g) (10 K)	H_C (Oe) (10 K)	SAR (W/g) (600 Oe)
41 ± 6	8.7	56 ± 1	61 ± 1	85 ± 2	154 ± 2	121.6
70 ± 12	8.0	54 ± 1	59 ± 1	83 ± 2	159 ± 2	101.2
107 ± 18	8.5	55 ± 1	61 ± 1	90 ± 2	159 ± 2	119.3
136 ± 16	8.8	53 ± 1	60 ± 1	89 ± 2	140 ± 2	122.3
201 ± 14	7.9	55 ± 1	62 ± 1	92 ± 2	134 ± 2	116.5
307 ± 28	7.6	52 ± 1	59 ± 1	88 ± 2	144 ± 2	105.6

oxygen was accounted for by assigning it to the remainder of the sample mass to calculate the atomic ratio. The compositional results from EDS closely matched those from ICP–MS. The theoretical formula from chemical synthesis is expected to be Ni_{0.5}Zn_{0.5}Fe₂O₄ with the use of 5 mmol of FeCl₃·6H₂O, 1.25 mmol of NiCl₂, and 1.25 mmol of ZnCl₂. The Ni/Fe ratios were close to the theoretical ratio of 0.25 from chemical synthesis, with values ranging from 0.23 to 0.25 according to EDS and 0.26 to 0.27 according to ICP–MS, suggesting that Ni²⁺ was completely incorporated into the spinel structures. For Zn²⁺, both EDS and ICP–MS results indicated that the Zn concentration in the sample diameter of 41 nm was the lowest, with a Zn/Fe ratio of about 0.1, while for other samples, the ratio ranged from 0.13 to 0.16. This discrepancy suggests that only a portion of Zn²⁺ was successfully incorporated into the spinel structures. The chemical formulas were deduced and are presented in Table 1. Given that ICP–MS provides more accurate analytical results, the experimental chemical formula derived from ICP–MS was used as the conclusive chemical formula for NZF NPs. The chemical formula for the 41 nm sample was estimated to be approximately Ni_{0.6}Zn_{0.2}Fe_{2.2}O₄, while other sizes had a comparably similar chemical formula of approximately Ni_{0.6}Zn_{0.3}Fe_{2.1}O₄.

Magnetic Properties of NZF Nanoparticles. The magnetic properties of all NZF NP samples were first assessed

through magnetization versus field $M(H)$ measurements at different temperatures. Figure 4a,b display the $M(H)$ curves obtained at 300 and 10 K for the representative samples with particle diameters of 41 ± 6 nm and 307 ± 28 nm (the smallest and largest particle size samples), respectively. The values of saturation magnetization (M_s) derived from the $M(H)$ curves are plotted against particle diameter (see Figure 4c). Table 2 summarizes the magnetic parameters of the NZF NPs. Owing to the small size of the primary crystals, ~8 nm (below the SPM size, ~20 nm), all samples are anticipated to exhibit SPM features at room temperature, with comparable values of M_s achieved across all particle sizes.³⁴ Indeed, at high temperatures (e.g., 300 and 350 K), the $M(H)$ curves of all samples exhibit zero values of remanent magnetization (M_r) and coercive field (H_C), a typical characteristic of superparamagnetism, (refer to Figures 4a,b, S2, and S3). Despite significant differences in the size of the NZF NPs, the M_s values were mostly comparable among the samples measured at 350 and 300 K (Figure 4c), underscoring the dominant influence of crystallite size in the NZF NP system. The magnetic properties at the low temperature of 10 K are also preserved across the size range, see Figures 4c and S4. Given similar M_s values attained above room temperature, nearly identical SAR values ranging from 100 to 120 W/g are also achieved, as discussed in the subsequent section. Accordingly,

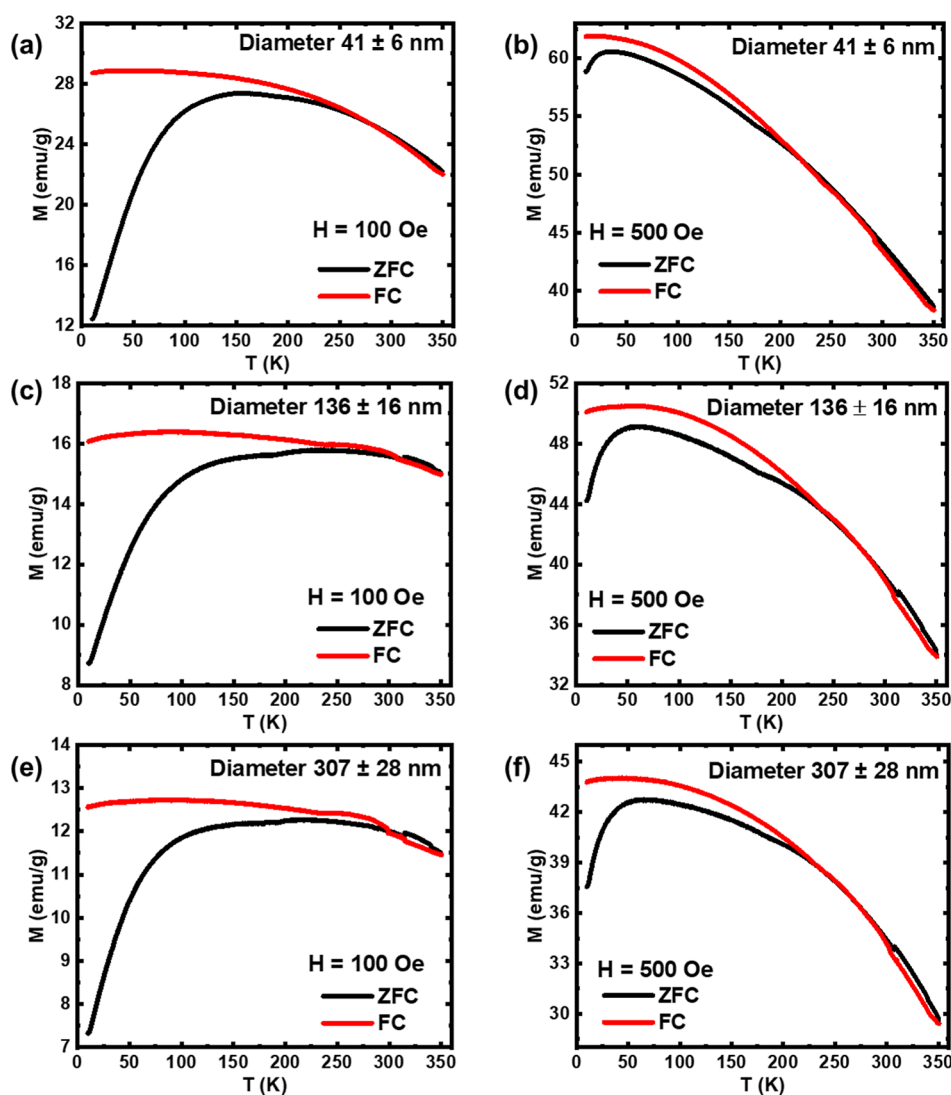


Figure 5. Temperature dependence of magnetization $M(T)$ at the fields of 100 and 500 Oe for NPs with average diameters of (a,b) 41 ± 6 nm, (c,d) 136 ± 16 nm, and (e,f) 307 ± 28 nm, respectively.

it can be concluded that the desirable magnetic properties of the NZF NPs are effectively preserved across a broad range of particle diameters, by controlling their crystallite sizes, which fundamentally plays a dominant role in the magnetic behavior of magnetic NPs.

To understand more deeply the magnetic properties of the NZF NPs, temperature-dependent magnetization ($M(T)$) measurements following the zero-field-cooled/field-cooled (ZFC-FC) protocol at two different applied fields of 100 and 500 Oe were conducted. The $M(T)$ curves of NZF NPs with diameters of 41 ± 6 nm, 136 ± 16 nm, and 307 ± 28 nm at the fields of 100 and 500 Oe are presented in Figure 5, while $M(T)$ data for other samples are shown in Figure S5. It can be seen in Figure 5a,c,e that at the lower field of 100 Oe, the $M(T)$ curve displays a broader ZFC peak with a more pronounced flattening over a larger temperature range as the diameter of the NZF NPs increases. In this NZF NP system, the clustering of primary nanocrystals forms large particles, with each polycrystalline particle being considered as a multispin nanocluster system. Consequently, there are multiple magnetic interactions, including intra- and interparticle interactions between nanocrystals within a particle, as well as interactions

among particles.^{47–50} The effects of size distribution, encompassing both the size distribution of nanocrystals forming a particle and of all particles within a sample, could also be significant. Therefore, the broadening feature of the ZFC $M(T)$ curves observed in our samples can be attributed to the size distribution of the crystals and particles, as well as the multiple magnetic interactions occurring within each particle and among particles.³³ Due to the multitude of factors influencing the broadening of ZFC $M(T)$ curves, deriving a definite value for the average blocking temperature (T_B) from this data is challenging and might lack precision. If defining the T_B as the temperature at which maximum magnetization occurs in ZFC conditions, as is typically used for single-domain SPM NPs,^{17,51} the T_B value can be estimated to be around 140 to 240 K due to the broadened features in the maximum magnetization region in ZFC observed at 100 Oe.

A more accurate approach to estimate the T_B of these samples involves examining the temperature-dependent coercive field derived from the $M(H)$ curves obtained at specific temperatures.³⁴ Here, the T_B is defined as the temperature at which the coercivity reaches zero upon temperature increase (see Figure 6). It is interesting that a

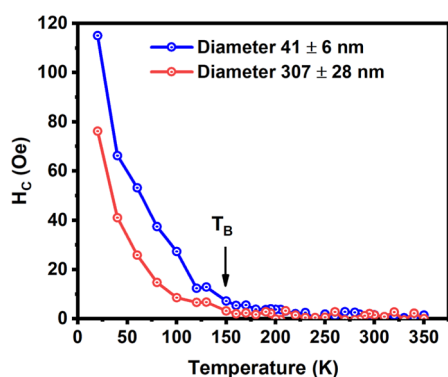


Figure 6. Coercivity versus temperature for NZF NPs of particle diameters 41 ± 6 and 307 ± 28 nm.

consistent value T_B at around 150 K was observed in the smallest and the largest samples. The value of T_B is highly sensitive to particle size and typically shifts to a larger value for larger particle sizes.⁵² In this case, the consistent T_B value in the smallest and the largest samples is driven by the similar crystallite size of the samples. Thus, the value of T_B in this particle system is size-independent. These findings reiterate the complexity involved in determining the average blocking temperatures of magnetic polycrystalline nanoparticle systems with multiple interactions solely from ZFC $M(T)$ data, unlike conventional magnetic nanoparticle systems. Surprisingly, our study focused on the SPM properties of polycrystalline Fe_3O_4 NPs also observed an identical T_B value of around 150 K in samples with sizes around 160 and 375 nm.³⁴

The $M(T)$ data taken at the higher field of 500 Oe provide additional insights into this phenomenon (see Figures 5b,d,f and S5). Due to the predominant influence of crystallite size, the substantial field of 500 Oe imposes a significant force to align the spin of the nanocrystals, leading to a similar $M(T)$ shape across all samples spanning from 41 to 307 nm. This consistent behavior is attributed to the similarity in the size of the primary crystals (crystallite size, ~ 8 nm). The maxima of the ZFC curves are positioned at approximately 35, 39, 56, 60, 63, and 65 K for sample diameters of 41 ± 6 , 70 ± 12 , 107 ± 18 , 136 ± 16 , 201 ± 14 , and 307 ± 28 nm, respectively. This slight shift in the ZFC maxima may suggest a stronger magnetic interaction among crystals within the larger particle structures. It is particularly intriguing to note from Table 2 that all samples display similar values of M_S (approximately 60 emu/g) and demonstrate outstanding SPM characteristics at

room temperature, despite variations in particle diameter ranging from 40 to 300 nm. These remarkable properties make them highly desirable for various biomedical applications, including magnetic hyperthermia therapy. To date, it is worth noting that the consistency of magnetic properties across the broad range of particle sizes is uniquely observed in this work.

Notably, the similarity in magnetic properties suggests that Néel relaxation remains largely invariant with particle size (driven by similar crystallite size), while Brownian relaxation, which is more size-dependent, might exhibit variations.⁵³ This distinctive feature could be exploited in MRI and biosensing, where Brownian relaxation and Néel relaxation are critical parameters influencing the response of NPs.^{54,55} Additionally, in biosensing applications, where magnetic NPs are used as magnetic markers to conjugate with biomolecules, the selection of an appropriate particle size not only enhances sensitivity, but also improves selectivity.⁵⁶ The observed phenomenon highlights potential opportunities for advanced biomedical applications by enabling new functionalities in nanoparticle-based technologies.

Magnetic Hyperthermia Applications. Magnetic hyperthermia refers to a therapeutic technique that utilizes magnetic NPs to generate heat within targeted tissues when exposed to an alternating magnetic field.⁵⁷ This localized heating can be precisely controlled and used to destroy cancer cells or treat other medical conditions, making magnetic hyperthermia a promising approach in oncology and other fields of medicine.⁵⁸ A wide range of ferrite NPs has been explored for this application.^{59–62}

To evaluate the potential uses of our SPM NZF NPs for magnetic hyperthermia therapy, the heating efficiency of all samples was assessed at a concentration of 1 mg/mL in water under different AC fields of 400 and 600 Oe, and the results are displayed in Figure 7. Figure 7a depicts the heating response of the NZF NPs to an AC magnetic field of 400 Oe, showing a continuous temperature increase during the application of the AC magnetic field. These heating curves were utilized to calculate the SAR, which is a measure of heating efficiency. Figure 7b illustrates the relationship between the size of the NZF NPs and SAR values in different AC fields. At both AC fields of 400 and 600 Oe, almost identical heating performances were observed for samples ranging from 41 to 307 nm. Figure 7c illustrates the consistent preservation of both SAR and M_S of NZF NPs across a wide size range. These important findings highlight the important role of controlling crystallite size (below the SPM size limit) in

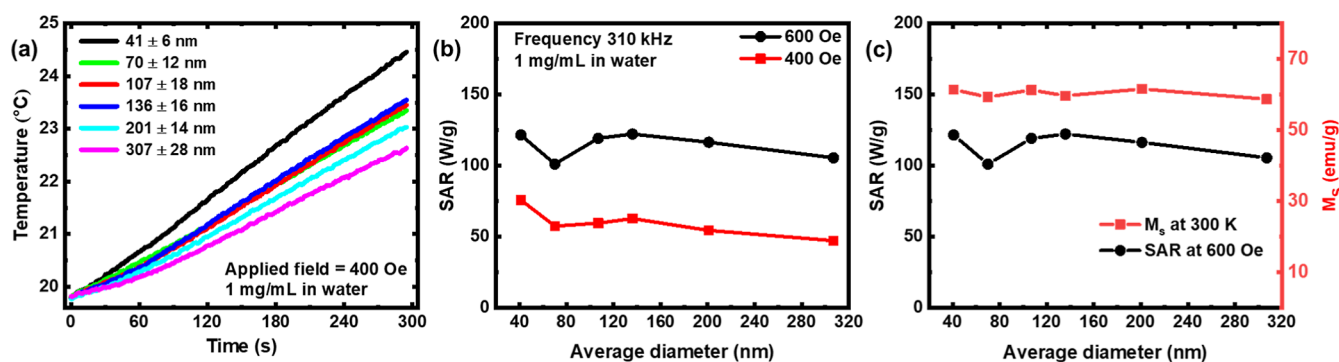


Figure 7. (a) Heating response of NZF NPs under an AC magnetic field; (b) relationship between the diameter of NZF NPs and SAR values at various AC fields; and (c) comparison of particle diameter with M_S and SAR values.

polycrystalline magnetic nanoparticle systems such as NZF NPs to achieve both SPM characteristics and comparable M_S and SAR values while tuning the particle diameter over a wide range spanning from 40 to 300 nm. Such nanostructures can fulfill specific applications ranging from advanced magnetic hyperthermia to targeted drug delivery and single particle-based biodetection.

Table S4 summarizes the results from previous magnetic hyperthermia studies on NZF NPs,^{13,18,28,30,63–66} detailing particle size and compositions, concentration of magnetic NPs, and AC field parameters. Although the hyperthermia experiments were not standardized in terms of consistency in frequency, AC field magnitude, and concentrations across different studies, to facilitate a reasonable comparison among studies, the conditions and samples resulting in the highest SAR in each study are displayed in Table S4. This table is designed to systematically present the latest advancements in the field and to provide a framework for outlining future studies involving NZF NPs. Its purpose is not for direct comparison but rather to facilitate a comprehensive understanding of the current progress and to guide future research directions in this area. While earlier research has investigated the magnetic hyperthermia responses of NZF NPs under diverse synthesis conditions,^{13,18,28,30,63,64} our study marks the first instance of demonstrating that NZF NPs can attain desirable superparamagnetism and comparable M_S across a broad range of particle diameters, spanning from 40 to 300 nm.

While the magnetic hyperthermia of NZF NPs has been the subject of several previous studies,^{13,18,19,25,28,30,63,64} this work uniquely investigates the magnetic hyperthermia properties of SPM NZF NPs in the large size range of 40 to 300 nm, demonstrating a desirable hyperthermia response. Generally, the magnetic hyperthermia response can be influenced by factors such as particle size and shape, solution concentration, composition, and the frequency and strength of the AC field.⁶⁷ Rhee's group provided a comprehensive study examining the hyperthermia performance of three compositions: $\text{Ni}_{0.8}\text{Zn}_{0.2}\text{Fe}_2\text{O}_4$, $\text{Ni}_{0.6}\text{Zn}_{0.4}\text{Fe}_2\text{O}_4$, and $\text{Ni}_{0.4}\text{Zn}_{0.6}\text{Fe}_2\text{O}_4$, at various concentrations ranging from 2 to 10 mg/mL and different fields from 1.65 to 4.40 kA/m at a fixed frequency of 216 kHz. The highest efficiency was observed for $\text{Ni}_{0.8}\text{Zn}_{0.2}\text{Fe}_2\text{O}_4$ at a concentration of 2 mg/mL and a field of 4.4 kA/m. The heating performance of NZF NPs in Kim's group's study exceeded that of our NZF NPs;¹³ however, the particle concentration in their hyperthermia experiments was three times higher. At a similar concentration of 1 mg/mL, the SAR values reported by Kim's group ranged from 120 to 144 W/g,¹³ which is comparable to our NZF NPs. Ramana et al. documented the magnetic hyperthermia of NZF NPs with chemical compositions similar to ours; their reported SAR value for $\text{Ni}_{0.60}\text{Zn}_{0.35}\text{Fe}_{2.05}\text{O}_4$ NPs was slightly lower than that of our NZF NPs, despite using a concentration that was 12 times higher.³⁰ Studies using similar NP concentrations of 1 mg/mL, such as those involving $\text{Zn}_{0.1}\text{Mn}_{0.9}\text{Fe}_2\text{O}_4$ and $\text{Ca}_{0.1}\text{Mg}_{0.9}\text{Fe}_2\text{O}_4$, reported SAR values in a range comparable to our materials.^{65,66} Compared to other studies, we highlighted the uniqueness of our nanoparticle system for hyperthermia, with tunable particle sizes that offer a desirable and comparable hyperthermia response across a broad size range.

While water is the standard biological medium for hyperthermia testing, an agar medium helps to minimize the physical movement of SPM NPs and mimics the viscous

cellular medium, such as the extracellular matrix or cell cytoplasm, akin to in vivo conditions.⁶⁸ The heating generated by magnetic NPs is contributed by Brownian motion, related to their physical movement under field manipulation, and by Néel magnetic moment relaxation.⁵⁷ Most magnetic hyperthermia studies have been conducted in a water medium. Recently, we found that the study by Parekh's group was the first to investigate the hyperthermia properties of NPs in an agarose medium for $\text{Mn}_{1-x}\text{Zn}_x\text{Fe}_2\text{O}_4$ NPs.⁶⁹ We conducted experiments to evaluate the hyperthermia properties of NZF NPs in agar medium, as shown in Figure S6, to enhance the understanding of the magnetic hyperthermia properties of this nanoparticle system. The SAR values of NZF NPs of different sizes showed more fluctuation compared to those recorded in a water medium, which could be explained by the difficulty in uniformly dispersing large-sized NPs in an agarose medium. The highest SAR value was observed for the sample with the smallest size, 41 nm, which could be attributed to the effective dispersion of the smallest NPs in a highly viscous medium. By measuring the hyperthermia response in agar to mitigate the heating contribution from Brownian motion, it could be inferred that the smallest NZF NPs might be slightly more efficient in magnetic hyperthermia.

CONCLUSIONS

Solvothermal synthesis, employing a pressure vessel, was utilized to fabricate polycrystalline nickel–zinc ferrite nanoparticles with the capability of broadly tuning the size while preserving both superparamagnetism and hyperthermia capabilities. The superparamagnetic properties and comparable saturation magnetization and hyperthermia performances were achieved across a diameter range of 40 to 300 nm, attributed to the similarity in the size of the primary crystals (crystallite size, ~ 8 nm) within the polycrystalline structures of the NZF NPs. Our study presents a strategic approach to preserving the excellent SPM properties ($M_S \sim 60$ emu/g at 300 K) and inductive heating capabilities (SAR values of ~ 100 to 120 W/g) of polycrystalline nanoparticle systems across a broad range of particle sizes through precise control of their crystallite sizes. The heating efficiency of the NZF NPs was thoroughly assessed at a low concentration of 1 mg/mL under various AC field conditions and dispersion media (water and agar) to simulate different biological environments. Additionally, a comprehensive analysis of the magnetic properties of the NZF NPs, including $M(H)$ at 10 and 350 K, $M(T)$ ZFC-FC at applied fields of 100 and 500 Oe, and H_C as a function of temperature, has also provided valuable insights into the intricate nature of multiple magnetic interactions within polycrystalline magnetic nanosystems and their distinctive blocking temperature characteristics. The insights into magnetism and hyperthermia gained from our study could serve as a valuable foundation for further designing magnetic nanoparticle structures for specific applications.

ASSOCIATED CONTENT

Supporting Information

The Supporting Information is available free of charge at <https://pubs.acs.org/doi/10.1021/acsami.5c00830>.

Calculated crystallite sizes of NZF NPs (Table S1); deconvolution of XRD peak to observe minor (222) peak (Figure S1); composition analysis by SEM-EDS (Table S2) and ICP–MS (Table S3); magnetic field

dependence of magnetization $M(H)$ at 350 K (Figure S2), 300 K (Figure S3), and 10 K (Figure S4); temperature dependence of magnetization $M(T)$ following ZFC-FC protocols at applied fields of 100 and 500 Oe (Figure S5); heating response of NZF NPs in agar medium (Figure S6); and listing of publications of NZF NPs for magnetic hyperthermia in aqueous media (Table S4) (PDF)

AUTHOR INFORMATION

Corresponding Authors

Manh-Huong Phan – Department of Physics, University of South Florida, Tampa, Florida 33620, United States; orcid.org/0000-0002-6270-8990; Email: phanm@usf.edu

T. Randall Lee – Department of Chemistry and the Texas Center for Superconductivity, University of Houston, Houston, Texas 77204-5003, United States; orcid.org/0000-0001-9584-8861; Email: trlee@uh.edu

Authors

Minh Dang Nguyen – Department of Chemistry and the Texas Center for Superconductivity, University of Houston, Houston, Texas 77204-5003, United States; orcid.org/0000-0002-2569-8279

Supun B. Attanayake – Department of Physics, University of South Florida, Tampa, Florida 33620, United States; orcid.org/0000-0003-0799-7889

Pailinrut Chinwangso – Department of Chemistry and the Texas Center for Superconductivity, University of Houston, Houston, Texas 77204-5003, United States; orcid.org/0009-0001-0691-8969

Supawitch Hoijang – Department of Chemistry and the Texas Center for Superconductivity, University of Houston, Houston, Texas 77204-5003, United States; orcid.org/0000-0002-0061-5166

Chengzhen Qin – Department of Electrical and Computer Engineering and the Texas Center for Superconductivity, University of Houston, Houston, Texas 77204-4005, United States

Jiming Bao – Department of Electrical and Computer Engineering and the Texas Center for Superconductivity, University of Houston, Houston, Texas 77204-4005, United States; orcid.org/0000-0002-6819-0117

Complete contact information is available at: <https://pubs.acs.org/10.1021/acsami.5c00830>

Notes

The authors declare no competing financial interest.

ACKNOWLEDGMENTS

T. R. Lee thanks for financial support from the Air Force Office of Scientific Research (FA9550-23-1-0581; 23RT0567) and the Robert A. Welch Foundation (grant no. E-1320 and V-E-0001). M. H. Phan acknowledges financial support from the US Department of Energy, Office of Basic Energy Sciences, Division of Materials Science and Engineering (Grant no. DE-FG02-07ER46438).

REFERENCES

- (1) Dippong, T.; Levei, E. A.; Cadar, O. Recent Advances in Synthesis and Applications of MFe_2O_4 ($M = Co, Cu, Mn, Ni, Zn$) Nanoparticles. *Nanomaterials* **2021**, *11*, 1560.
- (2) Amiri, M.; Salavati-Niasari, M.; Akbari, A. Magnetic Nano-carriers: Evolution of Spinel Ferrites for Medical Applications. *Adv. Colloid Interface Sci.* **2019**, *265*, 29–44.
- (3) Kefeni, K. K.; Msagati, T. A. M.; Nkambule, T. T. I.; Mamba, B. B. Spinel Ferrite Nanoparticles and Nanocomposites for Biomedical Applications and Their Toxicity. *Mater. Sci. Eng., C* **2020**, *107*, 110314.
- (4) Thakur, P.; Taneja, S.; Chahar, D.; Ravelo, B.; Thakur, A. Recent Advances on Synthesis, Characterization and High Frequency Applications of Ni-Zn Ferrite Nanoparticles. *J. Magn. Magn. Mater.* **2021**, *530*, 167925.
- (5) Leary, A. M.; Ohodnicki, P. R.; McHenry, M. E. Soft Magnetic Materials in High-Frequency, High-Power Conversion Applications. *JOM* **2012**, *64*, 772–781.
- (6) Konwar, K.; Bora, M.; Kaushik, S. D.; Chaturvedi, A.; Kumar, D.; Dutta, A.; Mukhopadhyay, R.; Babu, P. D.; Sharma, P.; Lodha, S.; Sen, D.; Ajayan, P. M.; Deb, P. $Ni_{1-x}Zn_xFe_2O_4@CoO$ ($x = 0.25$ and 0.50) Nanoparticles for Magnetic Resonance Imaging. *ACS Appl. Nano Mater.* **2023**, *6*, 20440–20457.
- (7) Kershi, R. M.; Alsheri, A. M.; Attiyah, R. M. Preparation of Ni-Zn Ferrite Nanoparticles and Study of Their Properties for Optoelectronic Applications. *J. Phase Equilib. Diffus.* **2024**, *45*, 900.
- (8) Adsure, K. T.; Jagtap, S. B.; Newaskar, S. R.; Kore, K. B.; Funde, A. M.; Patange, S. M.; Late, D. J. Exploring the Synthesis, Characterization, Electrical, and Magnetic Behavior of Crystalline $Ni_{1-x}Zn_xFe_2O_4$ Nanoparticles. *J. Mater. Sci.: Mater. Electron.* **2024**, *35*, 1714.
- (9) Maqsood, A.; Rehman, A. U.; Mahmood, A. Microstructural, Magnetic, and Optical Properties of Nickel-Doped Spinel Zinc Ferrite Nanoparticles. *Ceram. Int.* **2025**, *51*, 1732–1742.
- (10) Jangra, S.; Thakur, P.; Singh, S.; Thakur, A. Frequency and Temperature Dependent Impedance Studies: Impact of Cobalt Substitution on Ni-Zn Ferrites for High Frequency Applications. *Inorg. Chem. Commun.* **2025**, *174*, 113948.
- (11) Wang, J.; Ren, F.; Yi, R.; Yan, A.; Qiu, G.; Liu, X. Solvothermal Synthesis and Magnetic Properties of Size-Controlled Nickel Ferrite Nanoparticles. *J. Alloys Compd.* **2009**, *479*, 791–796.
- (12) Mallick, A.; Dey, C. C.; Sadhukhan, S.; Das, S.; Ningthoujam, R. S.; Greneche, J.-M.; Kumar Chakrabarti, P. Microwave Absorption and Hyperthermia Properties of Titanium Dioxide–Nickel Zinc Copper Ferrite Nanocomposite. *J. Magn. Magn. Mater.* **2023**, *587*, 171373.
- (13) Manohar, A.; Chintagumpala, K.; Kim, K. H. Mixed Zn–Ni Spinel Ferrites: Structure, Magnetic Hyperthermia and Photocatalytic Properties. *Ceram. Int.* **2021**, *47*, 7052–7061.
- (14) Dey, B.; Manoharan, C.; Venkateshwarlu, M.; Pawar, C. S.; Sagadevan, S. Exploring the Effect of Zinc Substitution in Nanocrystalline Nickel Ferrite for Enhanced Supercapacitor and Gas Sensing Applications. *Ceram. Int.* **2024**, *50*, 12121–12135.
- (15) Mao, J.; Hou, X.; Huang, F.; Shen, K.; Lam, K.; Ru, Q.; Hu, S. Zn Substitution $NiFe_2O_4$ Nanoparticles with Enhanced Conductivity as High-Performances Electrodes for Lithium Ion Batteries. *J. Alloys Compd.* **2016**, *676*, 265–274.
- (16) Sreekandan, S.; Thadathil, A.; Mavila, B.; Vellayan, K.; Periyat, P. Solvent-Free Synthesis of 1,2-Dihydro-1-Arylnaphtho[1,2-*e*] [1,3] Oxazine-3-Ones Using a Magnetic Nickel–Zinc Ferrite Nanocatalyst. *RSC Adv.* **2025**, *15*, 4553–4561.
- (17) Nguyen, M. D.; Tran, H.-V.; Xu, S.; Lee, T. R. Fe_3O_4 Nanoparticles: Structures, Synthesis, Magnetic Properties, Surface Functionalization, and Emerging Applications. *Appl. Sci.* **2021**, *11*, 11301.
- (18) Kahmei, R. D. R.; Seal, P.; Borah, P. Tunable heat generation in nickel-substituted zinc ferrite nanoparticles for magnetic hyperthermia. *Nanoscale Adv.* **2021**, *3*, 5339–5347.

- (19) Tovstolytkin, A. I.; Kulyk, M. M.; Kalita, V. M.; Ryabchenko, S. M.; Zamorskyi, V. O.; Fedorchuk, O. P.; Solopan, S. O.; Belous, A. G. Nickel-Zinc Spinel Nanoferrites: Magnetic Characterization and Prospects of the Use in Self-Controlled Magnetic Hyperthermia. *J. Magn. Magn. Mater.* **2019**, *473*, 422–427.
- (20) Bajorek, A.; Berger, C.; Dulski, M.; Lopadczak, P.; Zubko, M.; Prusik, K.; Wojtyniak, M.; Chrobak, A.; Grasset, F.; Randrianantoandro, N. Microstructural and Magnetic Characterization of Ni_{0.5}Zn_{0.5}Fe₂O₄ Ferrite Nanoparticles. *J. Phys. Chem. Solids* **2019**, *129*, 1–21.
- (21) Chakrabarty, S.; Bandyopadhyay, S.; Pal, M.; Dutta, A. Sol-Gel Derived Cobalt Containing Ni–Zn Ferrite Nanoparticles: Dielectric Relaxation and Enhanced Magnetic Property Study. *Mater. Chem. Phys.* **2021**, *259*, 124193.
- (22) Ghayour, H.; Abdellahi, M.; Ozada, N.; Jabrzare, S.; Khandan, A. Hyperthermia Application of Zinc Doped Nickel Ferrite Nanoparticles. *J. Phys. Chem. Solids* **2017**, *111*, 464–472.
- (23) Džunuzović, A. S.; Ilić, N. I.; Vijatović Petrović, M. M.; Bobić, J. D.; Stojadinović, B.; Dohčević-Mitrović, Z.; Stojanović, B. D. Structure and Properties of Ni–Zn Ferrite Obtained by Auto-Combustion Method. *J. Magn. Magn. Mater.* **2015**, *374*, 245–251.
- (24) Hwang, J.; Choi, M.; Shin, H.-S.; Ju, B.-K.; Chun, M. Structural and Magnetic Properties of NiZn Ferrite Nanoparticles Synthesized by a Thermal Decomposition Method. *Appl. Sci.* **2020**, *10*, 6279.
- (25) Arinzehukwu, C. E.; Aisida, S. O.; Agbogu, A.; Ahmad, I.; Ezema, F. I. Polyethylene Glycol Capped Nickel–Zinc Ferrite Nanocomposites: Structural, Optical and Magnetic Properties Suitable for Hyperthermia Applications. *Appl. Phys. A: Mater. Sci. Process.* **2022**, *128*, 1088.
- (26) Kumar, R.; Barman, P. B.; Singh, R. R. An Innovative Direct Non-Aqueous Method for the Development of Co Doped Ni-Zn Ferrite Nanoparticles. *Mater. Today Commun.* **2021**, *27*, 102238.
- (27) Gubbala, S.; Nathani, H.; Koizol, K.; Misra, R. D. K. Magnetic Properties of Nanocrystalline Ni–Zn, Zn–Mn, and Ni–Mn Ferrites Synthesized by Reverse Micelle Technique. *Phys. B* **2004**, *348*, 317–328.
- (28) Ahmad, A.; Bae, H.; Rhee, I.; Hong, S. Magnetic Heating of Triethylene Glycol (TREG)-Coated Zinc-Doped Nickel Ferrite Nanoparticles. *J. Magn. Magn. Mater.* **2018**, *447*, 42–47.
- (29) Kavas, H.; Baykal, A.; Toprak, M. S.; Köseoğlu, Y.; Sertkol, M.; Aktaş, B. Cation Distribution and Magnetic Properties of Zn Doped NiFe₂O₄ Nanoparticles Synthesized by PEG-Assisted Hydrothermal Route. *J. Alloys Compd.* **2009**, *479*, 49–55.
- (30) Ramana, P. V.; Rao, K. S.; Kumar, K. R.; Kapusetti, G.; Choppadandi, M.; Kiran, J. N.; Rao, K. H. A Study of Uncoated and Coated Nickel-Zinc Ferrite Nanoparticles for Magnetic Hyperthermia. *Mater. Chem. Phys.* **2021**, *266*, 124546.
- (31) Morrison, S. A.; Cahill, C. L.; Carpenter, E. E.; Calvin, S.; Swaminathan, R.; McHenry, M. E.; Harris, V. G. Magnetic and Structural Properties of Nickel Zinc Ferrite Nanoparticles Synthesized at Room Temperature. *J. Appl. Phys.* **2004**, *95*, 6392–6395.
- (32) Abd-Elnaiem, A. M.; Hakamy, A.; Afify, N.; Omer, M.; Abdelbaki, R. F. Nanoarchitectonics of Zinc Nickel Ferrites by the Hydrothermal Method for Improved Structural and Magnetic Properties. *J. Alloys Compd.* **2024**, *984*, 173941.
- (33) Nguyen, M. D.; Deng, L.; Lee, J. M.; Resendez, K. M.; Fuller, M.; Hoijsang, S.; Robles Hernandez, F. C.; Chu, C.-W.; Litvinov, D.; Hadjiev, V. G.; Xu, S.; Phan, M.-H.; Lee, T. R. Magnetic Tunability via Control of Crystallinity and Size in Polycrystalline Iron Oxide Nanoparticles. *Small* **2024**, *20*, 2402940.
- (34) Attanayake, S. B.; Nguyen, M. D.; Chanda, A.; Alonso, J.; Orue, I.; Lee, T. R.; Srikanth, H.; Phan, M.-H. Superparamagnetic Superparticles for Magnetic Hyperthermia Therapy: Overcoming the Particle Size Limit. *ACS Appl. Mater. Interfaces* **2025**, DOI: 10.1021/acsami.4c22386.
- (35) Xuan, S.; Wang, Y.-X. J.; Yu, J. C.; Cham-Fai Leung, K. Tuning the Grain Size and Particle Size of Superparamagnetic Fe₃O₄ Microparticles. *Chem. Mater.* **2009**, *21*, 5079–5087.
- (36) Yang, X.; Jiang, W.; Liu, L.; Chen, B.; Wu, S.; Sun, D.; Li, F. One-Step Hydrothermal Synthesis of Highly Water-Soluble Secondary Structural Fe₃O₄ Nanoparticles. *J. Magn. Magn. Mater.* **2012**, *324*, 2249–2257.
- (37) Liu, Y.; Cui, T.; Li, Y.; Zhao, Y.; Ye, Y.; Wu, W.; Tong, G. Effects of Crystal Size and Sphere Diameter on Static Magnetic and Electromagnetic Properties of Monodisperse Fe₃O₄ Microspheres. *Mater. Chem. Phys.* **2016**, *173*, 152–160.
- (38) Sharifi, I.; Shokrollahi, H.; Amiri, S. Ferrite-Based Magnetic Nanofluids Used in Hyperthermia Applications. *J. Magn. Magn. Mater.* **2012**, *324*, 903–915.
- (39) Li, X.; Li, Q.; Xia, Z.; Yan, W. Effects on Direct Synthesis of Large Scale Mono-Disperse Ni_{0.5}Zn_{0.5}Fe₂O₄ Nanosized Particles. *J. Alloys Compd.* **2008**, *458*, 558–563.
- (40) Lazarević, Z. Ž.; Milutinović, A. N.; Jovalekić, Č. D.; Ivanovski, V. N.; Daneu, N.; Mađarević, I.; Romčević, N. Ž. Spectroscopy Investigation of Nanostructured Nickel–Zinc Ferrite Obtained by Mechanochemical Synthesis. *Mater. Res. Bull.* **2015**, *63*, 239–247.
- (41) Jadhav, J.; Biswas, S.; Yadav, A. K.; Jha, S. N.; Bhattacharyya, D. Structural and Magnetic Properties of Nanocrystalline NiZn Ferrites: In the Context of Cationic Distribution. *J. Alloys Compd.* **2017**, *696*, 28–41.
- (42) Gómez, C. A. P.; Meneses, C. A. B.; Jaén, J. A. Raman Infrared and Mössbauer Spectroscopic Studies of Solid-State Synthesized Ni-Zn Ferrites. *J. Magn. Magn. Mater.* **2020**, *505*, 166710.
- (43) Grosvenor, A. P.; Biesinger, M. C.; Smart, R. St. C.; McIntyre, N. S. New Interpretations of XPS Spectra of Nickel Metal and Oxides. *Surf. Sci.* **2006**, *600*, 1771–1779.
- (44) Qu, L.; Wang, Z.; Hou, X.; Mao, J.; Wang, S.; Sun, G.; Wu, Y.; Liu, X. Rose Flowers” Assembled from Mesoporous NiFe₂O₄ Nanosheets for Energy Storage Devices. *J. Mater. Sci.: Mater. Electron.* **2017**, *28*, 14058–14068.
- (45) Medhi, R.; Li, C.-H.; Lee, S. H.; Marquez, M. D.; Jacobson, A. J.; Lee, T.-C.; Lee, T. R. Uniformly Spherical and Monodisperse Antimony- and Zinc-Doped Tin Oxide Nanoparticles for Optical and Electronic Applications. *ACS Appl. Nano Mater.* **2019**, *2*, 6554–6564.
- (46) Grosvenor, A. P.; Kobe, B. A.; Biesinger, M. C.; McIntyre, N. S. Investigation of Multiplet Splitting of Fe 2p XPS Spectra and Bonding in Iron Compounds. *Surf. Interface Anal.* **2004**, *36*, 1564–1574.
- (47) Fabris, F.; Tu, K.-H.; Ross, C. A.; Nunes, W. C. Influence of Dipolar Interactions on the Magnetic Properties of Superparamagnetic Particle Systems. *J. Appl. Phys.* **2019**, *126*, 173905.
- (48) Branquinho, L. C.; Carrião, M. S.; Costa, A. S.; Zufelato, N.; Sousa, M. H.; Miotto, R.; Ivkov, R.; Bakuzis, A. F. Effect of Magnetic Dipolar Interactions on Nanoparticle Heating Efficiency: Implications for Cancer Hyperthermia. *Sci. Rep.* **2013**, *3*, 2887.
- (49) Blanco-Mantecón, M.; O’Grady, K. Interaction and Size Effects in Magnetic Nanoparticles. *J. Magn. Magn. Mater.* **2006**, *296*, 124–133.
- (50) Frey, N. A.; Phan, M. H.; Srikanth, H.; Srinath, S.; Wang, C.; Sun, S. Interparticle Interactions in Coupled Au–Fe₃O₄ Nanoparticles. *J. Appl. Phys.* **2009**, *105*, 07B502.
- (51) Kolhatkar, A. G.; Jamison, A. C.; Litvinov, D.; Willson, R. C.; Lee, T. R. Tuning the Magnetic Properties of Nanoparticles. *Int. J. Mol. Sci.* **2013**, *14*, 15977–16009.
- (52) Park, J.; An, K.; Hwang, Y.; Park, J.-G.; Noh, H.-J.; Kim, J.-Y.; Park, J.-H.; Hwang, N.-M.; Hyeon, T. Ultra-Large-Scale Syntheses of Monodisperse Nanocrystals. *Nat. Mater.* **2004**, *3*, 891–895.
- (53) Ma, Z.; Mohapatra, J.; Wei, K.; Liu, J. P.; Sun, S. Magnetic Nanoparticles: Synthesis, Anisotropy, and Applications. *Chem. Rev.* **2023**, *123*, 3904–3943.
- (54) Zhou, Z.; Yang, L.; Gao, J.; Chen, X. Structure–Relaxivity Relationships of Magnetic Nanoparticles for Magnetic Resonance Imaging. *Adv. Mater.* **2019**, *31*, 1804567.
- (55) Haun, J. B.; Yoon, T.-J.; Lee, H.; Weissleder, R. Magnetic Nanoparticle Biosensors. *Wiley Interdiscip. Rev.: Nanomed. Nanobiotechnol.* **2010**, *2*, 291–304.

- (56) Chen, Y.-T.; Medhi, R.; Nekrashevich, I.; Litvinov, D.; Xu, S.; Lee, T. R. Specific Detection of Proteins Using Exceptionally Responsive Magnetic Particles. *Anal. Chem.* **2018**, *90*, 6749–6756.
- (57) Gavilán, H.; Avugadda, S. K.; Fernández-Cabada, T.; Soni, N.; Cassani, M.; Mai, B. T.; Chantrell, R.; Pellegrino, T. Magnetic Nanoparticles and Clusters for Magnetic Hyperthermia: Optimizing Their Heat Performance and Developing Combinatorial Therapies to Tackle Cancer. *Chem. Soc. Rev.* **2021**, *50*, 11614–11667.
- (58) Lavorato, G. C.; Das, R.; Alonso Masa, J.; Phan, M.-H.; Srikanth, H. Hybrid Magnetic Nanoparticles as Efficient Nanoheaters in Biomedical Applications. *Nanoscale Adv.* **2021**, *3*, 867–888.
- (59) Ge, X.; Mohapatra, J.; Silva, E.; He, G.; Gong, L.; Lyu, T.; Madhogaria, R. P.; Zhao, X.; Cheng, Y.; Al-Enizi, A. M.; Nafady, A.; Tian, J.; Liu, J. P.; Phan, M.-H.; Taraballi, F.; Pettigrew, R. I.; Ma, S. Metal–Organic Framework as a New Type of Magneto-thermally-Triggered On-Demand Release Carrier. *Small* **2024**, *20*, 2306940.
- (60) Phong, L. T. H.; Manh, H.; Nam, P. H.; Lam, V. D.; Khuyen, B. X.; Tung, B. S.; Bach, T. N.; Tung, D. K.; Phuc, N. X.; Hung, T. V.; Mai, T. L.; Phan, T. L.; Phan, M. H.; Phan, H.; Structural, M. Structural, magnetic and hyperthermia properties and their correlation in cobalt-doped magnetite nanoparticles. *RSC Adv.* **2022**, *12*, 698–707.
- (61) Lavorato, G. C.; Das, R.; Xing, Y.; Robles, J.; Litterst, F. J.; Baggio-Saitovitch, E.; Phan, M.-H.; Srikanth, H. Origin and Shell-Driven Optimization of the Heating Power in Core/Shell Bimagnetic Nanoparticles. *ACS Appl. Nano Mater.* **2020**, *3*, 1755–1765.
- (62) Das, R.; Alonso, J.; Nemati Porshokouh, Z.; Kalappattil, V.; Torres, D.; Phan, M.-H.; Garaio, E.; García, J. A. C.; Sanchez Llamazares, J. L.; Srikanth, H. Tunable High Aspect Ratio Iron Oxide Nanorods for Enhanced Hyperthermia. *J. Phys. Chem. C* **2016**, *120*, 10086–10093.
- (63) Kim, H. J.; Choi, H. Effect of Plasma Treatment on Magnetic Properties and Heating Efficiency of Ni-Zn Nanoparticles. *J. Magn. Mater.* **2019**, *484*, 14–20.
- (64) Rabi, B.; Ounacer, M.; Essoumhi, A.; Sajjeddine, M.; Ferreira, L. P.; Costa, B. F. O. Heating Efficiency of $\text{Ni}_{1-x}\text{Zn}_x\text{Fe}_2\text{O}_4$ Magnetic Nanoparticles. *J. Alloys Compd.* **2023**, *930*, 167241.
- (65) Manohar, A.; Vijayakanth, V.; Chintagumpala, K.; Manivasagan, P.; Jang, E.-S.; Kim, K. H. Zn-Doped MnFe_2O_4 Nanoparticles for Magnetic Hyperthermia and Their Cytotoxicity Study in Normal and Cancer Cell Lines. *Colloids Surf., A* **2023**, *675*, 132037.
- (66) Manohar, A.; Vijayakanth, V.; Vattikuti, S. V. P.; Manivasagan, P.; Jang, E.-S.; Chintagumpala, K.; Kim, K. H. Ca-Doped MgFe_2O_4 Nanoparticles for Magnetic Hyperthermia and Their Cytotoxicity in Normal and Cancer Cell Lines. *ACS Appl. Nano Mater.* **2022**, *5*, 5847–5856.
- (67) Guardia, P.; Di Corato, R.; Lartigue, L.; Wilhelm, C.; Espinosa, A.; Garcia-Hernandez, M.; Gazeau, F.; Manna, L.; Pellegrino, T. Water-Soluble Iron Oxide Nanocubes with High Values of Specific Absorption Rate for Cancer Cell Hyperthermia Treatment. *ACS Nano* **2012**, *6*, 3080–3091.
- (68) Serantes, D.; Simeonidis, K.; Angelakeris, M.; Chubykalo-Fesenko, O.; Marciello, M.; Morales, M.; Baldomir, D.; Martinez-Boubeta, C. Multiplying Magnetic Hyperthermia Response by Nanoparticle Assembling. *J. Phys. Chem. C* **2014**, *118*, 5927–5934.
- (69) Bhardwaj, A.; Parekh, K. Auto Tunable Hyperthermic Response of Temperature Sensitive Magnetic Fluid in Agarose Gel Containing $\text{Mn}_{1-x}\text{Zn}_x\text{Fe}_2\text{O}_4$ Nanoparticles. *J. Alloys Compd.* **2024**, *978*, 173407.